Draft version March 15, 2024
Typeset using LaTeX **twocolumn** style in AASTeX631

Realistic Uncertainties for Fundamental Properties of Asteroseismic Red Giants and the Interplay Between Mixing Length, Metallicity and $\nu_{\rm max}$

Yaguang Li (李亚光) ,[1,2] Timothy R. Bedding,[2] Daniel Huber,[1,2] Dennis Stello,[3,2] Jennifer van Saders,[1] Courtney L. Crawford,[2] Meridith Joyce,[4,5] Tanda Li (李坦达) ,[6] Simon J. Murphy,[7] K. R. Sreenivas,[2] and Yixiao Zhou (周一啸) [8]

[1]*Institute for Astronomy, University of Hawai'i, 2680 Woodlawn Drive, Honolulu, HI 96822, USA*
[2]*Sydney Institute for Astronomy (SIfA), School of Physics, University of Sydney, NSW 2006, Australia*
[3]*School of Physics, University of New South Wales, 2052, Australia*
[4]*Konkoly Observatory, HUN-REN Research Centre for Astronomy and Earth Sciences, Konkoly-Thege Miklós út 15-17, H-1121, Budapest, Hungary*
[5]*CSFK, MTA Centre of Excellence, Budapest, Konkoly-Thege Miklós út 15-17, H-1121, Budapest, Hungary*
[6]*Department of Astronomy, Beijing Normal University, Haidian District, Beijng 100875, China*
[7]*Centre for Astrophysics, University of Southern Queensland, Toowoomba, QLD 4350, Australia*
[8]*Stellar Astrophysics Centre, Department of Physics and Astronomy, Aarhus University, Ny Munkegade 120, DK-8000 Aarhus C, Denmark*

ABSTRACT

Asteroseismic modelling is a powerful way to derive stellar properties. However, the derived quantities are limited by built-in assumptions used in stellar models. This work presents a detailed characterisation of stellar model uncertainties in asteroseismic red giants, focusing on the mixing-length parameter $\alpha_{\rm MLT}$, the initial helium fraction $Y_{\rm init}$, the solar abundance scale, and the overshoot parameters. First, we estimate error floors due to model uncertainties to be ≈0.4% in mass, ≈0.2% in radius, and ≈17% in age, primarily due to the uncertain state of $\alpha_{\rm MLT}$ and $Y_{\rm init}$. The systematic uncertainties in age exceed typical statistical uncertainties, suggesting the importance of their evaluation in asteroseismic applications. Second, we demonstrate that the uncertainties from $\alpha_{\rm MLT}$ can be entirely mitigated by direct radius measurements or partially through $\nu_{\rm max}$. Utilizing radii from *Kepler* eclipsing binaries, we determined the $\alpha_{\rm MLT}$ values and calibrated the $\alpha_{\rm MLT}$–[M/H] relation. The correlation observed between the two variables is positive, consistent with previous studies using 1-D stellar models, but in contrast with outcomes from 3D simulations. Third, we explore the implications of using asteroseismic modelling to test the $\nu_{\rm max}$ scaling relation. We found that a perceived dependency of $\nu_{\rm max}$ on [M/H] from individual frequency modelling can be largely removed by incorporating the calibrated $\alpha_{\rm MLT}$–[M/H] relation. Variations in $Y_{\rm init}$ can also affect $\nu_{\rm max}$ predictions. These findings suggest that $\nu_{\rm max}$ conveys information not fully captured by individual frequencies, and that it should be carefully considered as an important observable for asteroseismic modelling.

Keywords: stars: solar-type – stars: oscillations (including pulsations) – stars: low-mass

1. INTRODUCTION

Asteroseismology has rapidly developed as a highly effective tool for determining the properties of field stars. Typical uncertainties of ≈4% in mass, ≈2% in radius, and ≈10% in age, are consistently reported in various studies for solar-type main-sequence stars and subgiants (e.g. Silva Aguirre et al. 2015, 2017; Li, T. et al. 2020). Similar levels of uncertainty, particularly precision, have also been indicated for red giants (Li, T. et al. 2022; Montalbán et al. 2021). This marks a significant advancement over traditional isochrone fitting methods, which typically yield uncertainties of ≈10% in mass and ≈50% in age (Tayar et al. 2022).

Given the promising results of asterseismology, the inherent systematic uncertainties in the underlying stellar models warrant careful examination. For example, a common practice in these models involves treating the mixing-length parameter $\alpha_{\rm MLT}$ and initial helium abundance $Y_{\rm init}$ as free variables, since neither of them can be precisely determined observationally for field stars (e.g. Lebreton & Goupil 2014; Appourchaux et al. 2015; Silva Aguirre et al. 2015). However, without proper

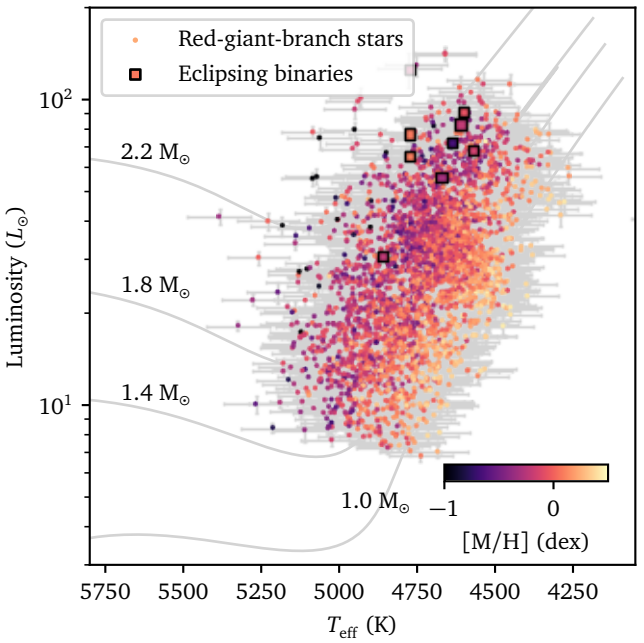

Figure 1. H–R diagram showing the sample used in this work, colour-coded by metallicity. A few solar-metallicity tracks are also shown for visual guidance.

constraints, this approach can inadvertently mask other model imperfections and lead to significant biases in the estimation of stellar properties (Cunha et al. 2021). This issue becomes critically important for Galactic archaeology, where age scales for millions of red giants have been calibrated based on asteroseismic datasets and the systematic uncertainties are often left unaccounted for (Ho et al. 2017; Wu et al. 2018; Wang et al. 2023a; Anders et al. 2023).

In this paper, we aim to scrutinize some of the systematic uncertainties in models, and highlight their significant contribution to the overall uncertainty in determining fundamental stellar properties, especially age, which often surpasses statistical uncertainties. We will assess their impact on estimating stellar properties (Section 3), investigate the interplay between $\alpha_{\rm MLT}$, radius and metallicity [M/H] (Section 4), and finally, discuss how these model uncertainties affect the validation of the $\nu_{\rm max}$ scaling relation (Section 5).

2. DATA ANALYSIS

2.1. *Observations*

We first describe the observational data used to constrain stellar models. In this work, we used the low-luminosity asteroseismic red-giant-branch (RGB) sample observed by *Kepler* (Yu et al. 2018). We selected low-luminosity stars (below about 100 L$_\odot$) by restricting $\nu_{\rm max}$ to be above 17μHz.

For asteroseismic inputs, we chose $\nu_{\rm max}$ values processed by the nuSYD pipeline (Sreenivas et al. 2024). This pipeline offers slightly improved precision compared to the SYD pipeline (Huber et al. 2009; Chontos et al. 2021; Yu et al. 2018), due to their simple treatment of granulation background and the low-level noise in their adopted PDCSAP (Pre-search Data Conditioning Simple Aperture Photometry) light curves (Stumpe et al. 2012; Smith et al. 2012). We used oscillation frequencies ($l = 0, 2$) extracted by Kallinger (2019), who followed a standard peakbagging approach. We also used $l = 1$ g-mode period spacings ($\Delta\Pi_1$) from Vrard et al. (2016), rather than the individual $l = 1$ oscillation frequencies, to avoid the complexity of treating mixed modes in stellar modelling (Ball et al. 2018).

For spectroscopic inputs, we used metallicity [M/H] from APOGEE (Abdurro'uf et al. 2022; Pinsonneault et al. 2018), and $T_{\rm eff}$ that we derived from the IRFM method (Casagrande et al. 2021), which uses *Gaia* and 2MASS photometry and extinction values from Green et al. (2019) as inputs. By comparing the IRFM $T_{\rm eff}$ and the APOGEE $T_{\rm eff}$ values, we observed a systematic variation: the IRFM $T_{\rm eff}$ is 50 K higher than the APOGEE values at [M/H] ~ -0.6 dex, and conversely, 50 K lower at [M/H] ~ 0.4 dex. The root-mean-square difference between the two $T_{\rm eff}$ sources is about 70 K across all [M/H] levels. We found that the choice of $T_{\rm eff}$ scale made little difference to our results (see Section 4).

We determined luminosities using K_s-band magnitudes (Cutri et al. 2003), along with Green et al. (2019) extinctions, Choi et al. (2016) bolometric corrections, and *Gaia* DR3 distances (Bailer-Jones et al. 2021).

Furthermore, we included oscillating eclipsing binaries analysed by Gaulme et al. (2016), Brogaard et al. (2018), and Benbakoura et al. (2021), which have masses and radii measured from dynamical modelling. In cases where a star was analysed by multiple studies, we opted for the parameters reported from the most recent study. Figure 1 presents the sample used in this work on the Hertzsprung-Russell diagram.

2.2. *Stellar models*

We constructed a new set of stellar models with MESA (version r15140; Paxton et al. 2011, 2013, 2015, 2018, 2019) and GRYE (version 6.0.1; Townsend & Teitler 2013). The construction of these models is largely based on the input physics outlined in Li, Y. et al. (2023). The convection was formulated with the mixing-length theory from Henyey et al. (1965) and the surface boundary conditions were constructed with Eddington $T - \tau$ grey atmosphere model (Eddington 1926). At the end of the

paper, we provided a link to the configuration files used for producing the MESA models.

There are two primary differences compared to the Li, Y. et al. (2023) models. Firstly, the new models considered possible variations in the convective overshoot. We used the exponential overshooting scheme according to Herwig (2000), and varied the amount of overshoot for core and shell convective boundaries independently as $f_{\rm ov,core} \in (0., 0.03)$ and $f_{\rm ov,shell} \in (0., 0.02)$, respectively. The other free parameters for the grid were initial stellar mass $M \in (0.6, 2.5)$, metallicity [M/H] $\in (-1.0, 0.6)$, the initial helium abundance $Y_{\rm init} \in (0.20, 0.37)$, and the mixing-length parameter $\alpha_{\rm MLT} \in (1.0, 2.7)$. No mass loss was included in the models.

Secondly, in addition to calculating the frequencies of the radial modes ($\ell = 0$) we also calculated frequencies of decoupled (pure p) quadrupolar modes ($\ell = 2$) using the method introduced by Ong & Basu (2020). We incorporated the $\ell = 2$ modes in this work because the spacing between $\ell = 0$ and $\ell = 2$ modes, the so-called small separation, relates closely to stellar mass in red giants and could offer extra constraints on stellar properties (Montalbán et al. 2010; Kallinger et al. 2012).

2.3. *Model fitting*

We followed the model-fitting framework described in Li, Y. et al. (2023). Each model is associated with global stellar parameters $\{M, R, L, {\rm Age}, \Delta\Pi_1, T_{\rm eff}, {\rm [M/H]}, ...\}$ and oscillation frequencies $\{\nu_i\}$. Following Li, Y. et al. (2023), we corrected the surface effect in $\{\nu_i\}$ with an ensemble approach, which helps eliminate unrealistic surface corrections and reduces scatter in model-derived properties. We achieved this by parameterizing the amount of surface correction at $\nu_{\rm max}$, $\delta\nu_{\rm m}$, and at 10% above $\nu_{\rm max}$, $\delta\nu'_m$, as functions of stellar surface properties:

$$\delta\nu_{\rm m} = a \cdot (g/g_\odot)^b \cdot (T_{\rm eff}/T_{\rm eff,\odot})^c \cdot (d \cdot {\rm [M/H]} + 1), \quad (1)$$

and

$$\delta\nu'_m = a' \cdot (g/g_\odot)^{b'} \cdot (T_{\rm eff}/T_{\rm eff,\odot})^{c'} \cdot (d' \cdot {\rm [M/H]} + 1). \quad (2)$$

These two equations were then used to determine the surface terms (a_{-1} and a_3) in the inverse-cubic correction formula (Ball & Gizon 2014):

$$\delta\nu(\nu; a_{-1}, a_3) = \left(a_{-1}\nu^{-1} + a_3\nu^3\right)/\mathcal{I}, \quad (3)$$

where $\mathcal{I}$ is the mode inertia. The parameters appearing in these equations, $\{a, b, c, d, a', b', c', d'\}$, were jointly fitted to the entire sample, yielding best-fitting values of $\{-6.11 \pm 0.28, 0.79 \pm 0.04, , -5.04 \pm 0.85, -0.79 \pm 0.09, -7.69 \pm 0.72, 0.79 \pm 0.03, -4.59 \pm 0.68, -0.87 \pm 0.08\}$. These values are slightly different from those reported by Li, Y. et al. (2023), due to the differences in underlying models and observational constraints, indicating the importance of such re-calibration for this method.

To determine stellar properties, we applied a range of observational constraints, quantified using chi-squared (χ^2) functions for goodness of fit:

$$\chi^2_q = \left(\frac{q_{\rm obs} - q_{\rm mod}}{\sigma_q}\right)^2, \quad (4)$$

where q represents the observables $\nu_{\rm max}$, $\Delta\Pi_1$, L, $T_{\rm eff}$, [M/H], M, and R. For individual frequencies, we used reduced χ^2 functions for a group of modes with the same ℓ-degree, which are the standard χ^2 functions averaged by the number of oscillation modes:

$$\chi^2_l = \frac{1}{N_l}\sum_i^{N_l}\left(\frac{\nu_{{\rm obs},l,i} - \nu_{{\rm mod},l,i}}{\sigma_{\nu_{{\rm obs},l,i}}}\right)^2. \quad (5)$$

In a strict statistical sense, using an average by the number of modes is not appropriate, because each frequency was determined independently. However, these χ^2 functions are very sensitive to inaccurate predictions of mode frequencies, due to the relatively small magnitudes of $\sigma_{\nu_{\rm obs}}$. Relying on a single set of grid models with a specific selection of input phyiscs (as was done in this work) is unable to fully capture all sources of systematic uncertainties. This limitation could result in extremely large values for the seismic χ^2 functions. Hence, the average method reduces the reliance of the seismic χ^2 on the inaccurate predictions, and quantitatively it is similar to adding an extra error term for systematic uncertainties. We refer the reader to Cunha et al. (2021) for a thorough discussion on this topic.

For illustration, we combine observational constraints into separate groups. The $\chi^2_{\rm freq}$ includes individual frequencies for modes of $l = 0$ and $l = 2$:

$$\chi^2_{\rm freq} = \chi^2_{l=0} + \chi^2_{l=2}. \quad (6)$$

The seismic constraint $\chi^2_{\rm seis}$ incorporates both individual frequencies and global seismic parameters ($\nu_{\rm max}$ and $\Delta\Pi_1$):

$$\chi^2_{\rm seis} = \chi^2_{\rm freq} + \chi^2_{\nu_{\rm max}} + \chi^2_{\Delta\Pi_1}. \quad (7)$$

The *Gaia* constraint applies to luminosity:

$$\chi^2_{\rm Gaia} = \chi^2_L, \quad (8)$$

and the spectroscopic constraint covers $T_{\rm eff}$ and [M/H]:

$$\chi^2_{\rm spec} = \chi^2_{T_{\rm eff}} + \chi^2_{\rm [M/H]}. \quad (9)$$

For the eclipsing binaries, the dynamical constraint includes mass and radius obtained from the modelling of the binary orbit:

$$\chi^2_{\rm dyn} = \chi^2_M + \chi^2_R. \quad (10)$$

When combining these individual constraints, we implicitly assume that each was derived independently, even though this may not be the case. For example, $T_{\rm eff}$ and [M/H] are often strongly correlated from spectroscopic analysis. To accurately account for such correlations, it is essential to include information on the covariance matrix (e.g. Gent et al. 2022). However, this information was not available for most of our sample.

Under the Bayesian model-fitting framework, the posterior probability for the model parameters is expressed as

$$p(\theta|\mathcal{D}) = p(\theta) \times \mathcal{L}(\mathcal{D}|\theta), \quad (11)$$

where $p(\theta)$ is the prior on model parameters, which are uniform within the grid boundaries unless noted otherwise. The likelihood function quantifies the agreement between models (specified by θ) and observational data ($\mathcal{D}$):

$$\mathcal{L}(\mathcal{D}|\theta) = \exp\left(-\chi^2/2\right), \quad (12)$$

where χ^2 includes various observational constraints that are detailed in subsequent sections. The estimation of a stellar parameter of interest was determined by integrating Eq. 11 over other model parameters, a process called marginalisation.

3. UNCERTAINTIES FROM MODEL INPUT PHYSICS

3.1. *Varying input physics*

When studying the effects of varying input physics, Lebreton et al. (2014) identified the most important factors contributing to the uncertainty in the main-sequence lifetime. These include chemical abundances, convective core overshoot, and rotation, with discrepancies surpassing 30% in comparison to a reference model. Chemical abundances and convective core overshoot are especially crucial for low-mass stars less than 1.7 $M_\odot$ (see also Ying et al. 2023; Joyce et al. 2023). In this section, we look deep into how variations in these two types of input physics influence the inferred stellar properties, in the context of using constraints from asteroseismology.

This investigation was done by adjusting key parameters in our models: the mixing-length parameter $\alpha_{\rm MLT}$, the initial helium fraction $Y_{\rm init}$, the solar abundance values $(Z/X)_\odot$ used in metallicity calculations, and the core overshoot parameter, $f_{\rm ov,core}$. Each star was fitted with the full set of observables: $\chi^2 = \chi^2_{\rm seis} + \chi^2_{\rm Gaia} + \chi^2_{\rm spec}$.

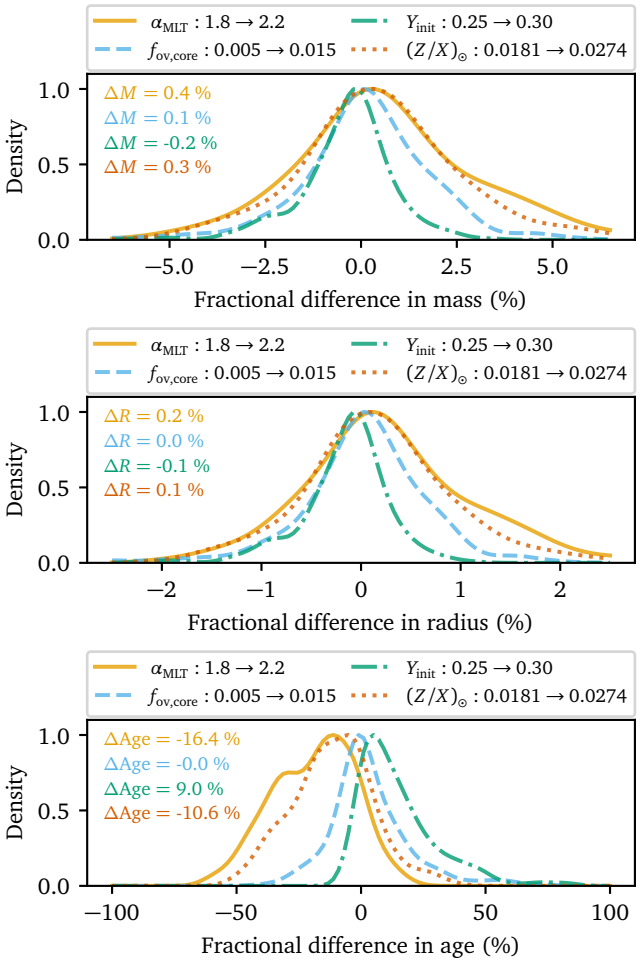

Figure 2. Distributions of the fractional differences in masses, radii, and ages for our red giant sample that result from changing the input physics. Each line corresponds to changing the values of a different model parameter (see legends), and the numbers indicate to the median differences. The distributions have been processed through Gaussian kernel density estimations for clearer visualization. The stellar properties shown in this diagram were derived with $\nu_{\ell=0}$, $\nu_{\ell=2}$, $\Delta\Pi_1$, $\nu_{\rm max}$, $T_{\rm eff}$, [M/H], and L.

We assessed the fractional differences in stellar properties resulting from these adjustments, with the distributions displayed in Figure 2.

A key focus was on the impact of varying $\alpha_{\rm MLT}$, which prescribes convective flux transport in convection zones and is especially important in super-adiabatic regions. Although solar-calibrated $\alpha_{\rm MLT}$ values are commonly used in stellar isochrones, several studies advocate for and validate non-solar values across diverse samples (see Joyce & Tayar 2023). In our analysis, we varied $\alpha_{\rm MLT}$ from 1.8 to 2.2, which covers the range commonly explored in these studies for red giants. The adjustment was implemented by modifying the priors in Eq. 11. For

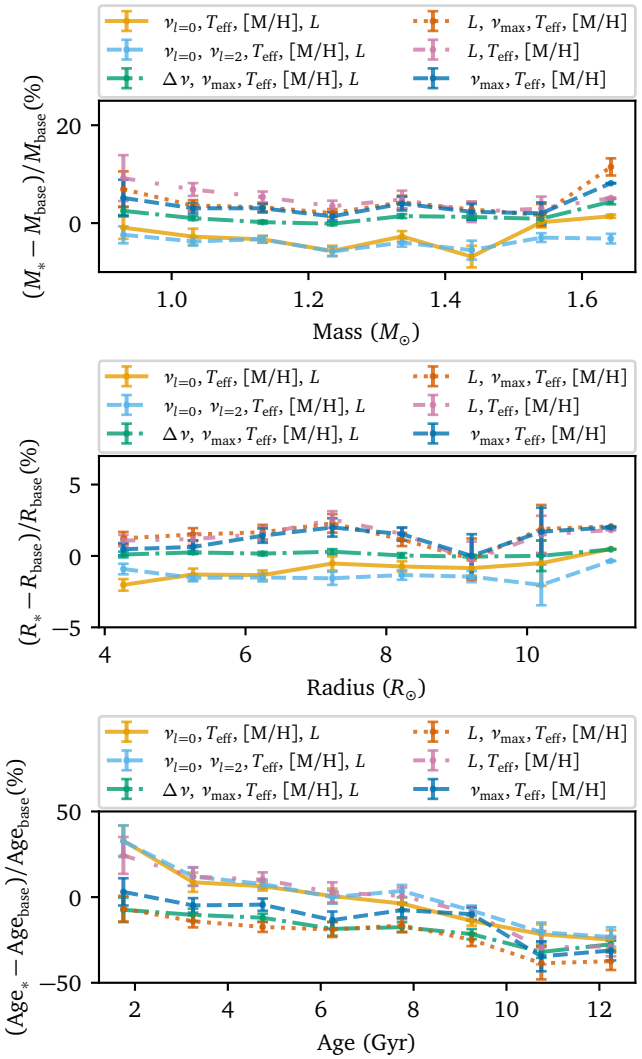

Figure 3. Changes in the derived masses, radii, and ages for our red giant sample that result from changing the input physics. Each point shows the binned medians and the associated errors on the binned medians. In each panel, the x-axis shows the stellar properties derived with $\nu_{\ell=0}$, $\nu_{\ell=2}$, $\Delta\Pi_1$, $\nu_{\rm max}$, $T_{\rm eff}$, [M/H], and L, denoted as the "base" case. They are compared against the stellar properties derived by other combinations of observational constraints (see legends).

example, setting $\alpha_{\rm MLT}$ to 1.8 involves applying the following normal distribution:

$$\alpha_{\rm MLT} \sim \mathcal{N}(1.8, \sigma), \tag{13}$$

where $\mathcal{N}(\mu, \sigma)$ denotes a normal distribution with mean μ and standard deviation σ. Here we chose σ as 0.05, and tests showed that using other values (0.025 and 0.1) did not lead to significant differences.

As can be seen from Figure 2, altering $\alpha_{\rm MLT}$ by 0.4 induces the largest variations among the tests we conducted. The median differences are 0.4% in mass, 0.2% in radius, and 16.4% in age. The pronounced $\alpha_{\rm MLT}$ effect on age is indirect, because an increased $\alpha_{\rm MLT}$ tends to favour models with different abundance values that modify ages directly. Specifically, the 0.4 increase in $\alpha_{\rm MLT}$ decreases $Y_{\rm init}$ by $\approx$0.08, leading to a reduced hydrogen burning rate on the main sequence (McKeever et al. 2019; Lebreton et al. 2014). Moreover, since the metal-to-hydrogen ratio ([M/H] or Z/X) is a fixed constant observational constraint, the change in $\alpha_{\rm MLT}$ raises both $X_{\rm init}$ (by $\approx$0.06) and $Z_{\rm init}$ (by $\approx$0.004). The increase in fuel and the higher opacity during the main sequence both prolong the main-sequence lifespan, substantially increasing the estimated stellar ages (see also Valle et al. 2018).

Next, we explored the effects of varying the initial helium abundance $Y_{\rm init}$. Due to the lack of photospheric helium lines, direct measurements of helium abundance are challenging, leading to $Y_{\rm init}$ often being treated as a free parameter in stellar modelling. In favorable cases, asteroseismology can measure the helium abundance in the stellar envelope by using the change of the adiabatic index in the HeII ionization zone, which produces oscillatory signatures in p-mode frequencies (Basu & Antia 2004; Broomhall et al. 2014; Verma et al. 2019; Dréau et al. 2020). In our analysis, we modified $Y_{\rm init}$ from 0.25 to 0.30, aligning with recent seismic estimations (McKeever et al. 2019; Ong et al. 2022). This was implemented by setting priors $Y_{\rm init} \sim \mathcal{N}(0.25, 0.03)$ and $\mathcal{N}(0.30, 0.03)$. The median differences observed are 0.2% in mass, 0.1% in radius, and 9.0% in age. The age discrepancies, although significant, were less pronounced than those caused by changes in $\alpha_{\rm MLT}$, as a result of a smaller range of variation in $Y_{\rm init}$ (0.05 in this case as opposed to 0.08).

We also examined the effect of different solar abundance scale $(Z/X)_\odot$ values. The metallicity ratio [M/H], derived from spectroscopy, implicitly sets a specific solar abundance value $(Z/X)_\odot$:

$$[\mathrm{M/H}] = \log_{10}(Z/X) - \log_{10}(Z/X)_\odot. \tag{14}$$

Various studies have measured $(Z/X)_\odot$ ranging between 0.0181 and 0.0274 (Anders & Grevesse 1989; Grevesse & Sauval 1998; Asplund et al. 2009). We tested the effects of these variations by altering the model definition of [M/H], as reflected in $\chi^2_{\rm spec}$. The resulting median differences are 0.3% in mass, 0.1% in radius, and 10.6% in age, showing a similar magnitude of impact as the adjustment in $Y_{\rm init}$.

Lastly, we assessed the effect of changing the core overshoot parameter $f_{\rm ov,core}$. In stars with masses greater than $\sim$ 1.2 $M_\odot$, $f_{\rm ov,core}$ plays a critical role in determining the convective core boundary and the mixing

within. Based on calibrations from asteroseismology and eclipsing binaries (Claret & Torres 2018; Deheuvels et al. 2016; Tian et al. 2015), we compared two values for $f_{\rm ov,core}$, using priors $f_{\rm ov,core} \sim \mathcal{N}(0.005, 0.005)$ and $\mathcal{N}(0.015, 0.005)$. The changes observed were minimal: negligible in both mass and radius, and 1.0% in age. We also did not find substantial impacts when changing $f_{\rm ov,shell}$, although its value is known to impact the position of the RGB bump (Christensen-Dalsgaard 2015; Khan et al. 2018).

3.2. *Varying the choices of observables*

We can gain further insights into the impact of uncertain input physics by comparing the stellar properties derived from different sets of observables. Figure 3 compares the properties derived using various observables against those obtained from the full set: $\chi^2 = \chi^2_{\rm seis} + \chi^2_{\rm Gaia} + \chi^2_{\rm spec}$.

Our first focus concerns models that incorporate asteroseismic constraints only from individual frequencies: $\nu_{\ell=0}$ and $\nu_{\ell=2}$. These models show discrepancies compared to those using the full set, with systematic offsets of up to 5% in mass, 1% in radius, and 15% in age. We also observed a discernible trend in the age discrepancies, correlating with the age itself. These discrepancies are attributed to the inclusion of $\nu_{\rm max}$ in the full set, which offers partial constraints on $\alpha_{\rm MLT}$ (discussed in Section 4), leading to a slightly different parameter scale.

We then considered models optimized only by global parameters. We confirmed there are substantial deviations when relying solely on L, $T_{\rm eff}$, and [M/H], as used in traditional isochrone fitting, with systematic offsets of up to 10% in mass, 2% in radius, and 30% in age, compared to those with the full inputs. When incorporating $\nu_{\rm max}$, either in addition to or as a replacement for L, the discrepancy in radius is similar but the divergence reduces to 5% in mass and by 15% in age. This is because $\nu_{\rm max}$ relates to mass with power of 1 (see Eq. 15). The inclusion of $\nu_{\rm max}$, especially for stars beyond 3 kpc where *Gaia* distance measurements are less precise, proves to be very beneficial in improving parameter accuracy (Huber et al. 2017). Furthermore, models incorporating $\Delta\nu$ as an input show excellent consistency with the full seismic inputs. Consequently, we recommend employing a combination of $\Delta\nu$ and $\nu_{\rm max}$ wherever possible, to fully maximize the accuracy of stellar properties (Silva Aguirre et al. 2020).

3.3. *Summary*

Our investigation reveals that the inherent uncertainties in stellar models can lead to significant deviations in the estimated properties of asteroseismic red giants. Specifically, we observed uncertainties up to ≈0.4% in mass, ≈0.2% in radius and, notably, ≈17% in age. The uncertainties mainly stem from the poorly-constrained helium abundance ($Y_{\rm init}$), which significantly influences other parameters such as the mixing-length parameter ($\alpha_{\rm MLT}$), initial hydrogen fraction ($X_{\rm init}$), and initial metallicity ($Z_{\rm init}$). The age uncertainty is particularly critical, often surpassing the statistical uncertainties commonly reported in individual frequency modelling, which are typically around ≈10% (Montalbán et al. 2021; Wang et al. 2023b).

Our results show that, despite integrating constraints from asteroseismic data, a baseline level of systematic uncertainty still persists. This systematic uncertainty sets a realistic lower limit for stellar properties. It is a crucial factor to consider in the application of asteroseismic data for stellar evolution and Galactic archaeology studies.

It is also important to note that, while our study primarily targets RGB stars, the uncertainties for red clump could be even higher due to the potential accumulation of errors during the earlier evolutionary phases of these stars (Cinquegrana et al. 2023).

4. CONSTRAINING THE MIXING-LENGTH PARAMETER

4.1. *Interplay between $\alpha_{\rm MLT}$, radius, and ν_{max}*

Our analysis of stellar models, when we omit $\nu_{\rm max}$ as a constraint and rely on $\chi^2 = \chi^2_{\rm freq} + \chi^2_{\rm Gaia} + \chi^2_{\rm spec}$, reveals a notable challenge in precisely determining stellar the radius. This difficulty stems from the lack of constraint on the mixing-length parameter ($\alpha_{\rm MLT}$). We explain this issue in greater detail below.

In the upper-left panel of Figure 4, we present the posterior distribution of KIC 9540226, marginalised over the $\alpha_{\rm MLT}$–radius parameter space. It reveals a strong negative and nearly linear correlation between the two parameters under the observational constraints, with a Pearson correlation coefficient of −0.43. The correlation suggests that accurate determination of either $\alpha_{\rm MLT}$ or radius is challenging without incorporating additional data.

In the upper-middle panel of Figure 4, we introduce an extra constraint, $\nu_{\rm max}$. Since our 1-D models do not predict amplitudes, the $\nu_{\rm max}$ values were calculated from the scaling relation:

$$\frac{\nu_{\rm max}}{\nu_{\rm max,\odot}} \approx \left(\frac{M}{M_\odot}\right)\left(\frac{R}{R_\odot}\right)^{-2}\left(\frac{T_{\rm eff}}{T_{\rm eff,\odot}}\right)^{-1/2}, \qquad (15)$$

where $\nu_{\rm max,\odot} = 3090$ μHz, and $T_{\rm eff,\odot} = 5772$ K (Kjeldsen & Bedding 1995). This inclusion visibly weakens

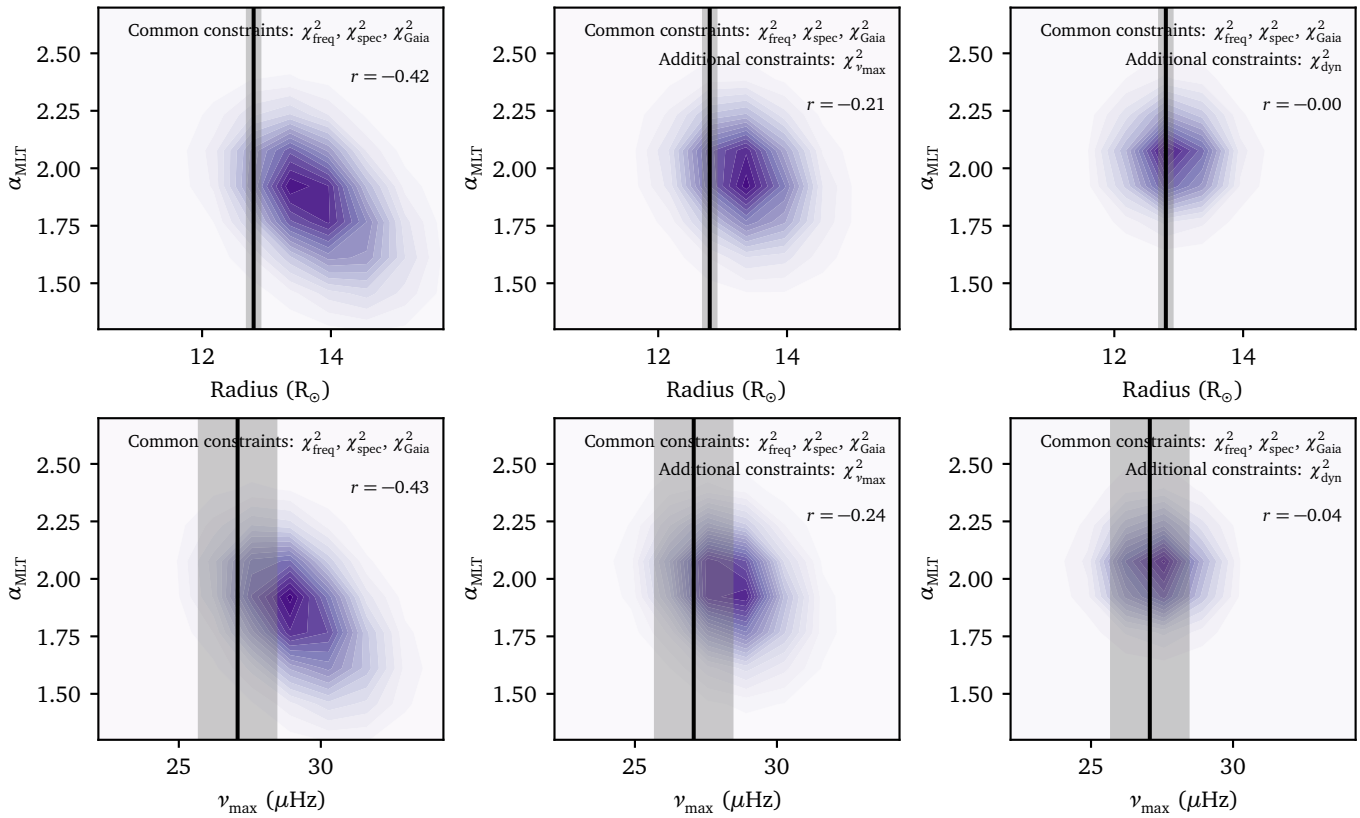

Figure 4. Posterior distributions for KIC 9540226 (an eclipsing binary) modelled with $\chi^2 = \chi^2_{\rm freq} + \chi^2_{\rm spec} + \chi^2_{\rm Gaia}$. The top panels show the distributions marginalised in the ($\alpha_{\rm MLT}$, radius) space and the bottom panels show those in the ($\alpha_{\rm MLT}$, $\nu_{\rm max}$) space. The panels in the middle column show the results with additional constraint of $\chi^2_{\nu_{\rm max}}$. The panels in the right column show those with additional constraint of $\chi^2_{\rm dyn}$. The Pearson correlation coefficients calculated from the distributions are displayed in each panel. The vertical lines and the shaded regions show the medians and 1-σ values for the measured radius (from binary modelling) and the measured $\nu_{\rm max}$ (from observed power spectra).

the correlation (Pearson correlation coefficient reduced to -0.21) because $\nu_{\rm max}$ is proportional to $MR^{-2}T_{\rm eff}^{-1/2}$, indirectly imposing a constraint on the radius.

In the upper-right panel of Figure 4, we applied additional constraints, $\chi^2_{\rm dyn}$, related to the mass and radius of KIC 9540266. This effectively neutralizes the correlation between $\alpha_{\rm MLT}$ and radius, allowing for a precise determination of $\alpha_{\rm MLT}$. Joyce & Chaboyer (2018a) applied a similar approach to the α Cen A & B binary system, demonstrating a relation between $\alpha_{\rm MLT}$ and stellar mass that was preserved across all variations in input physics. We also tested with the radius constraint alone, which yielded similar outcomes. This indicates the importance of direct radius measurements, such as those from interferometry and binary orbit modelling, for calibrating $\alpha_{\rm MLT}$ in stars beyond the Sun.

In the lower panels of Figure 4, we present the posterior distributions now marginalised over the $\alpha_{\rm MLT}$–$\nu_{\rm max}$ space. We found that precise $\nu_{\rm max}$ determination from models hinges on having $\alpha_{\rm MLT}$ calibrated with direct stellar radius data. It highlights an important point: predicting a reliable $\nu_{\rm max}$ value based solely on individual frequencies is nearly impractical without a predetermined $\alpha_{\rm MLT}$. This is because the individual frequencies are mostly sensitive to deeper regions within the star, and their sensitivity to super adiabatic near-surface regions is considerably reduced by the empirical surface correction procedure.

4.2. *Relation between $\alpha_{\rm MLT}$ and metallicity*

We now turn to examining the relationship between $\alpha_{\rm MLT}$ and [M/H]. It has been shown in previous studies (such as Metcalfe et al. 2014; Creevey et al. 2017; Tayar et al. 2017; Joyce & Chaboyer 2018b; Viani et al. 2018; Li, T. et al. 2018; Valle et al. 2019) that 1-D stellar models, when constrained by asteroseismic data, often require adjustments in the $\alpha_{\rm MLT}$ values depending the metallicity. This relationship is typically found as a monotonically increasing trend between the two parameters. However, this trend contrasts with findings from 3D hydrodynamic simulations of stellar surfaces (Magic et al. 2015). This discrepancy has been acknowledged

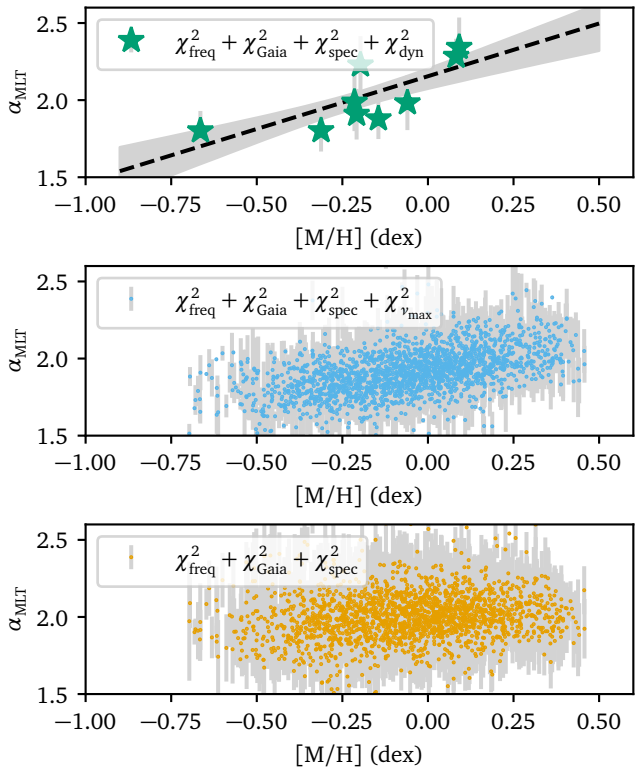

Figure 5. Derived relationships between $\alpha_{\rm MLT}$ and metallicity. The top panel shows the results modelled with the additional $\chi^2_{\rm dyn}$ from the binary sample. The middle panel shows those modelled with $\chi^2_{\nu_{\rm max}}$. The bottom panel shows those modelled without either of them.

by Tayar et al. (2017) and Viani et al. (2018) and the reason is not entirely clear.

We now revisit the $\alpha_{\rm MLT}$–[M/H] relation, which we intend to constrain with $\chi^2_{\rm dyn}$. The results are shown in Figure 5. With the $\chi^2_{\rm dyn}$ constraints (top panel), we still observe a positive correlation between $\alpha_{\rm MLT}$ and [M/H], akin to the pattern found in previous 1-D studies and in models constrained by $\chi^2_{\nu_{\rm max}}$ (middle panel). However, there is a slight difference in the correlation slopes when comparing the two methods. This variation can be attributed to the different effectiveness of $\chi^2_{\nu_{\rm max}}$ and $\chi^2_{\rm dyn}$ in mitigating the correlation between $\alpha_{\rm MLT}$ and radius, as previously discussed. When neither $\chi^2_{\rm dyn}$ nor $\chi^2_{\nu_{\rm max}}$ are employed (bottom panel), the correlation between $\alpha_{\rm MLT}$ and [M/H] almost vanishes. Hence, it is important to have effective constraints on $\alpha_{\rm MLT}$ for model-based parameter inference. Relying solely on models without such constraints could lead to a systematic bias in the derived stellar properties, as we discussed in Section 3.

Using the mass and radius measurements from the eclipsing binary sample, along with the spectroscopic and asteroseismic constraints, we fitted a linear relation between $\alpha_{\rm MLT}$ and [M/H]:

$$\alpha_{\rm MLT} = (0.66 \pm 0.20) \times [{\rm M/H}] + (2.14 \pm 0.06). \quad (16)$$

We verified these results by replacing $T_{\rm eff}$ values from those from APOGEE, and found a similar relation:

$$\alpha_{\rm MLT} = (0.60 \pm 0.14) \times [{\rm M/H}] + (2.14 \pm 0.06). \quad (17)$$

The slope of $\alpha_{\rm MLT}$ with respect to [M/H] agrees well with the findings of Viani et al. (2018), who modelled stars with $\Delta\nu$, $\nu_{\rm max}$, $T_{\rm eff}$, and [M/H] and reported a slope of ≈0.74. However, our value appears to be higher than the ≈0.16 value found by Tayar et al. (2017), which might be due to their focus on matching $T_{\rm eff}$ instead.

We investigated whether [M/H] is the primary driver for the variability of $\alpha_{\rm MLT}$ in red giants. We calculated the correlation coefficients of $\alpha_{\rm MLT}$ with respect to [M/H], mass, and $T_{\rm eff}$ for the binary sample. They are 0.75, 0.74, and 0.70, respectively, suggesting that a relation with mass or $T_{\rm eff}$ could be equally plausible. However, we have to keep in mind that the binary sample only spans a rather small parameter range. In contrast, for the large asteroseismic sample constrained by $\nu_{\rm max}$, we found those coefficients to be 0.46, 0.10, and 0.02, respectively. Assuming the $\nu_{\rm max}$-constrained scenario is accurate, then [M/H] is indeed the dominant factor influencing variations in $\alpha_{\rm MLT}$ for red giants.

Based on these findings, we adopt Eq. 16 as a preliminary model for further discussions in the subsequent section. We encourage future studies to further refine and validate this relationship as more data from similar systems become available. In particular, more calibrators at lower luminosities and higher metallicities will be especially helpful (see Figure 1).

5. IMPLICATIONS ON TESTING THE $\nu_{\rm max}$ SCALING RELATION

5.1. *Background*

The $\nu_{\rm max}$ scaling relation is an extremely useful tool for measuring stellar parameters, especially in the current era of extensive ensemble analysis of red giants. Despite its widespread use, the limitations and full scope of this relation are not completely understood (Hekker 2020). In this section, we attempt to test this scaling relation using 1-D stellar modelling.

The frequency of maximum power, $\nu_{\rm max}$, is governed by excitation and damping mechanisms, and is therefore inherently a surface property. In this sense, it is different from the individual modes frequencies, which are the resonant frequencies of the entire star. Given that solar-like oscillations are driven and damped by near-surface convection (Goldreich et al. 1994; Samadi et al. 2012;

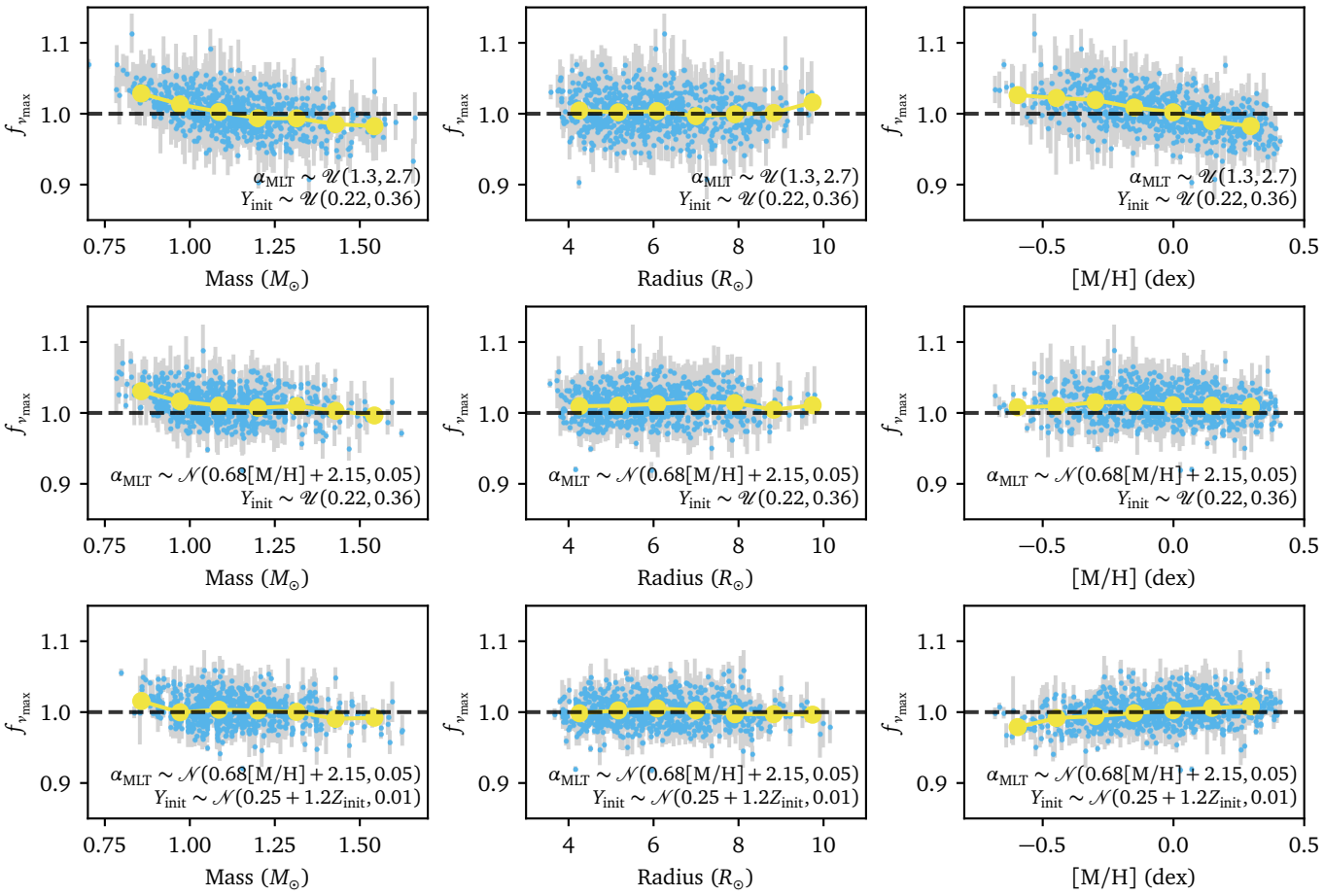

Figure 6. Correction factor of the $\nu_{\rm max}$ scaling relation, $f_{\nu_{\rm max}}$, as a function of mass, radius, and metallicity (from left to right panels). The top rows show the results obtained without imposing informative priors on $\alpha_{\rm MLT}$ and $Y_{\rm init}$. The middle rows show those with the calibrated $\alpha_{\rm MLT}$–[M/H] relation from the eclipsing binary sample. The bottom rows show those with an assumed helium enrichment law.

Zhou et al. 2020), it is reasonable to suppose that $\nu_{\rm max}$, like amplitude, is determined by the surface properties of stars, namely effective temperature, surface gravity and possibly metallicity.

The $\nu_{\rm max}$ scaling relation, originally proposed for main-sequence stars by Brown et al. (1991) and Kjeldsen & Bedding (1995), posits that $\nu_{\rm max}$ is a fixed fraction of the acoustic cutoff frequency ($\nu_{\rm ac}$) in the stellar atmosphere, which sets the upper boundary limit for sound waves to remain trapped within the star. Under assumptions of an isothermal atmosphere and ideal gas conditions[1], $\nu_{\rm ac}$ can be shown to scale as $\nu_{\rm ac} \propto g/\sqrt{T_{\rm eff}}$, where g is the surface gravity and $T_{\rm eff}$ is the effective temperature. To quantify deviation from the scaling relation, we can define a factor $f_{\nu_{\rm max}}$ as follows (Sharma et al. 2016):

$$\frac{\nu_{\rm max}}{\nu_{\rm max,\odot}} = f_{\nu_{\rm max}} \left(\frac{M}{M_\odot}\right) \left(\frac{R}{R_\odot}\right)^{-2} \left(\frac{T_{\rm eff}}{T_{\rm eff,\odot}}\right)^{-1/2} . \quad (18)$$

The $\nu_{\rm max}$ scaling relation has undergone extensive validation against various methodologies, such as astrometry-based luminosities (Silva Aguirre et al. 2012; Huber et al. 2017; Sahlholdt & Silva Aguirre 2018; Hall et al. 2019; Khan et al. 2019; Zinn et al. 2019), masses and radii from eclipsing binaries (Gaulme et al. 2016; Brogaard et al. 2018; Kallinger et al. 2018; Benbakoura et al. 2021), and the sharpness of population-level features, such as the zero-age main-sequence edge in red giants (Li, Y. et al. 2021).

Two interesting deviations have emerged in the extremes of parameter space. First, there is a noticeable deviation for red giants with radii larger than ≈50 $R_\odot$, which is expected since those stars experience a transition in driving mechanisms — from near-surface convection to an opacity-based heat engine (Yu et al.

[1] These are simplifications that, admittedly, aren't strictly accurate.

2020; Zinn et al. 2023). Second, there is a potentially unaccounted-for dependency of $\nu_{\rm max}$ on metallicity, supported by possible correlations seen in model-based stellar parameters (Li, T. et al. 2022; Wang et al. 2023b), and the tendency of $\nu_{\rm max}$-based stellar mass to be overestimated in metal-poor stars (Epstein et al. 2014; Schonhut-Stasik et al. 2023). An additional metallicity term could resolve these discrepancies.

Indeed, by using a more accurate derivation for sound speed, Viani et al. (2017) proposed that $\nu_{\rm ac}$ can also depend on the mean molecular weight and the adiabatic index, thereby introducing a metallicity component (see also Jiménez et al. 2015; Yıldız et al. 2016). However, recent 3D hydrodynamic atmosphere simulations by Zhou et al. (2023) did not reveal significant variations of $\nu_{\rm max}$ with metallicity, which could be due to a counteracting effect from the Mach number dependency, as suggested by Belkacem et al. (2011).

5.2. *Results and discussions*

We tested the $\nu_{\rm max}$ scaling relation using the individual frequency modelling approach, similar to prior studies including Metcalfe et al. (2014), Coelho et al. (2015), Li, T. et al. (2022) and Wang et al. (2023b). Our approach involves computing a scaling $\nu_{\rm max}$ according to Eq. 15, using observational properties other than $\nu_{\rm max}$ as constraints: $\chi^2 = \chi^2_{\rm freq} + \chi^2_{\rm Gaia} + \chi^2_{\rm spec}$. The derived scaling $\nu_{\rm max}$ is then compared against the actual measured $\nu_{\rm max}$ from power spectra. The ratio of the measured to the derived value is $f_{\nu_{\rm max}}$ (see Eq. 18). Our method differs from previous studies in two aspects: (1) we incorporate a more comprehensive list of observational constraints including $\ell = 0 - 2$ mode frequencies, to get more precise constraints on the internal structure; (2) we study how model uncertainties affect the derived $\nu_{\rm max}$.

Figure 6 presents the correction factor $f_{\nu_{\rm max}}$ as a function of mass, radius, and age. We also employ median values aggregated into bins (displayed as circles), to highlight any systematic trends in $f_{\nu_{\rm max}}$. Our initial analysis, presented in the top row of the figure, was conducted without applying informative priors on $\alpha_{\rm MLT}$ and $Y_{\rm init}$. These results indicate a negative correlation of $f_{\nu_{\rm max}}$ with both mass and metallicity. Such findings could lead to the conclusions that adjustments to the $\nu_{\rm max}$ scaling relation are necessary. The correlation with [M/H] is especially tempting, considering the previously discussed influence of [M/H].

However, it is essential to approach these trends cautiously. Our previous discussions suggest that $\alpha_{\rm MLT}$ is not adequately constrained even with asteroseismic frequencies. Thus, employing non-informative priors on $\alpha_{\rm MLT}$ can result in systematically biased stellar parameters. To address this, we used a normal prior on $\alpha_{\rm MLT}$ around the value given by Eq. 16:

$$\alpha_{\rm MLT} \sim \mathcal{N}(0.68[{\rm M/H}] + 2.15, 0.05). \tag{19}$$

The resulting $f_{\nu_{\rm max}}$ is shown in the middle row of Figure 6. The trend with [M/H] vanishes when we incorporate the calibrated $\alpha_{\rm MLT}$-[M/H] relation. The trend with mass also greatly reduces.

Interestingly in this case, we noticed that the $f_{\nu_{\rm max}}$ factor consistently exceeds 1, hinting at a possible need to adjust the reference values in Eq. 15 for red giants from the current solar-based values. Yet, this adjustment may not be necessary if we apply specific priors to $Y_{\rm init}$. We implemented a normal prior for $Y_{\rm init}$ based on the Galactic enrichment law:

$$Y_{\rm init} \sim \mathcal{N}(Y_p + \frac{\Delta Y}{\Delta Z} Z_{\rm init}, 0.01), \tag{20}$$

with $Y_p = 0.25$ and $\Delta Y/\Delta Z = 1.2$. Note that the exact values of this law are still debated in the literature (Jimenez et al. 2003; Casagrande et al. 2007; Verma et al. 2019). The outcomes of this implementation are shown in the bottom row of Figure 6. We observed that the $f_{\nu_{\rm max}}$ correction factor closely aligns with 1, suggesting no significant deviation from the standard scaling relation. We also note that in this case $f_{\nu_{\rm max}}$ presents a positive correlation with [M/H], which can be easily destructed again with a slightly different prescription for $\alpha_{\rm MLT}$.

From these findings, we conclude that testing the $\nu_{\rm max}$ scaling relation through individual frequency modelling does not always yield conclusive results and requires a thorough consideration of model uncertainties, especially $\alpha_{\rm MLT}$ and $Y_{\rm init}$. Additionally, we may also expect that other model assumptions, such as the atmosphere boundary condition (Choi et al. 2018; Salaris et al. 2018) and the treatment of surface correction (Li, Y. et al. 2023), modify the surface layers and influence the derived scaling $\nu_{\rm max}$.

Our findings also indicate that $\nu_{\rm max}$ imparts unique information distinct from individual frequencies. Therefore, $\nu_{\rm max}$ should be regarded as a valuable constraint in asteroseismic modelling.

5.3. *Recommendations for using the ν_{max} scaling relation*

We recommend practices for using $\nu_{\rm max}$ to derive stellar properties. Most $\nu_{\rm max}$ extraction pipelines only consider the statistical uncertainties for measuring $\nu_{\rm max}$, which sometimes could be smaller than the total error budget. Below we list some of the external sources of uncertainties.

First, the values of $\nu_{\rm max}$ is influenced by the method in which stellar oscillation was detected. $\nu_{\rm max}$ is affected by the wavelength range of the photometric filters used, as well as whether observations are conducted through radial velocity or photometry. Such factors can result in $\approx$5% discrepancies in $\nu_{\rm max}$ in the Sun (Howe et al. 2020). Moreover, differences in the treatment of power spectra among data reduction pipelines can lead to differences in $\nu_{\rm max}$ for about 2% (Pinsonneault et al. 2018). Therefore, when the studied samples are not characterised with the same instrument or the same data reduction pipeline, it is crucial to account for these additional sources of discrepancy.

Second, $\nu_{\rm max}$ changes over time due to astrophysical origins. For example, $\nu_{\rm max}$ is subject to variations with magnetic cycles. The Sun varies $\nu_{\rm max}$ of $\approx$0.8% in a solar cycle (Howe et al. 2020). In addition, the stochastic nature of oscillations can cause $\nu_{\rm max}$ to fluctuate over fixed lengths of observing windows. In the case of *Kepler* red giants, typical scatter in $\nu_{\rm max}$ ranges from 2% to 5% in three-month observing windows (Sreenivas et al. 2024). This issue is even more troublesome for some *TESS* stars with only one sector of data (e.g. Jiang et al. 2023). Hence, these types of uncertainties need to be quantified, presumably via simulations, especially if $\nu_{\rm max}$ is measured with short time series.

6. CONCLUSIONS

In our study, we present a detailed characterisation of red giant model uncertainties, focusing on the impact of the mixing-length parameter $\alpha_{\rm MLT}$, the initial helium fraction $Y_{\rm init}$, the solar abundance scale $(Z/X)_\odot$, and the core overshoot parameter $f_{\rm ov,core}$. Our objective is to understand how these factors influence the determination of stellar mass, radius, and age in asteroseismic modelling. The key conclusions are summarised as follows:

1. We identified that uncertainties in $\alpha_{\rm MLT}$ and $Y_{\rm init}$ significantly affect the accuracy of stellar properties, despite incorporating constraints from spectroscopy ($T_{\rm eff}$, [M/H]), *Gaia* astrometry (L), and asteroseismology ($\nu_{\ell=0}$, $\nu_{\ell=2}$, $\nu_{\rm max}$, $\Delta\Pi_1$). These uncertainties set an error floor on mass of $\approx$0.4%, radius of $\approx$0.2%, and age of $\approx$17% (Figure 2). The error floors due to model uncertainties in age exceed typical statistical uncertainties $\approx$10%, showing the importance of their evaluation in asteroseismic applications.

2. We examined the effect of different combinations of observational constraints (Figure 3). Incorporating asteroseismic constraints only from individual frequencies shows discrepancies compared to the case of using the full set of inputs that include $\nu_{\rm max}$, suggesting $\nu_{\rm max}$ sets a slightly different parameter scale, due to its constraining ability on $\alpha_{\rm MLT}$. In addition, incorporating asteroseismic constraints from $\Delta\nu$ and $\nu_{\rm max}$ shows excellent consistency with the full set of inputs. Therefore, for ensemble analysis of red giants, a combination of $\Delta\nu$ and $\nu_{\rm max}$ should be included wherever possible.

3. We showed that an uncertain state of $\alpha_{\rm MLT}$ translates to uncertain predictions on stellar radius and $\nu_{\rm max}$ (Figure 4). Hence, direct measurements of stellar radius will enable the calibration of $\alpha_{\rm MLT}$. Using the *Kepler* eclipsing binary sample, for which dynamical radii are available, we determined their $\alpha_{\rm MLT}$ values and provided a fitting relation between $\alpha_{\rm MLT}$ and [M/H] (Figure 5). The slope between $\alpha_{\rm MLT}$ and [M/H] is consistent with previous studies involving 1-D models but still in tension with 3D simulations.

4. We showed that predicting a reliable $\nu_{\rm max}$ value based solely on individual frequencies is nearly impractical (Figure 4). The model-derived scaling $\nu_{\rm max}$, shows strong dependence on the uncertainties in both $\alpha_{\rm MLT}$ and $Y_{\rm init}$, which prohibits accuracy tests on the $\nu_{\rm max}$ scaling relation from asteroseismic modelling (Figure 6). We noted that $\nu_{\rm max}$ provides distinct information and should be considered as an important observable in asteroseismic modelling. We provided our recommendations in Section .

ACKNOWLEDGEMENTS

Y.L. expresses gratitude to Bill Chaplin and Margarida Cunha for their thorough and constructive comments during his PhD exam process. Y.L. acknowledges the support by the Beatrice Watson Parrent Fellowship and the National Aeronautics and Space Administration (80NSSC19K0597). We acknowledge support from the Australian Research Council for T.R.B (DP210103119 and FL220100117), D.S. (DP190100666) and S.J.M (FT210100485). D.H. acknowledges support from the Alfred P. Sloan Foundation and the Australian Research Council (FT200100871). M.J. is supported by the Horizon 2020 research and innovation programme's funding of MATISSE: *Measuring Ages Through Isochrones, Seismology, and Stellar Evolution.*

Funding for the Kepler mission is provided by the NASA Science Mission Directorate. This paper includes data collected by the Kepler mission and obtained from the MAST data archive at the Space Telescope Science

Institute (STScI). STScI is operated by the Association of Universities for Research in Astronomy, Inc., under NASA contract NAS 5–26555.

This work presents results from the European Space Agency (ESA) space mission Gaia. Gaia data are being processed by the Gaia Data Processing and Analysis Consortium (DPAC). Funding for the DPAC is provided by national institutions, in particular the institutions participating in the Gaia MultiLateral Agreement (MLA).

The APOGEE data is from the Sloan Digital Sky Survey IV, whose funding has been provided by the Alfred P. Sloan Foundation, the U.S. Department of Energy Office of Science, and the Participating Institutions.

We acknowledge the Sydney Informatics, the University of Sydney's high performance computing (HPC) cluster Artemis, and the University of Hawaii's Information Technology Services – Cyberinfrastructure (funded in part by the National Science Foundation CC* awards #2201428 and #2232862), for providing the HPC resources that have contributed to the research results reported within this paper.

Software: Numpy (van der Walt et al. 2011), Scipy (Virtanen et al. 2020), Matplotlib (Hunter 2007), Astropy (Astropy Collaboration et al. 2013, 2018), Pandas (Wes McKinney 2010), MESA (Paxton et al. 2011, 2013, 2015, 2018, 2019), MESASDK (Townsend 2020), GYRE (Townsend & Teitler 2013), Lightkurve (Lightkurve Collaboration et al. 2018), ISOCLASSIFY (Huber et al. 2017; Berger et al. 2020), colte (Casagrande et al. 2021), GPT-4 (OpenAI 2023). The scripts and MESA inlists used in this work are available at GitHub[2].

REFERENCES

Abdurro'uf, Accetta, K., Aerts, C., et al. 2022, ApJS, 259, 35, doi: 10.3847/1538-4365/ac4414

Anders, E., & Grevesse, N. 1989, GeoCoA, 53, 197, doi: 10.1016/0016-7037(89)90286-X

Anders, F., Gispert, P., Ratcliffe, B., et al. 2023, A&A, 678, A158, doi: 10.1051/0004-6361/202346666

Appourchaux, T., Antia, H. M., Ball, W., et al. 2015, A&A, 582, A25, doi: 10.1051/0004-6361/201526610

Asplund, M., Grevesse, N., Sauval, A. J., & Scott, P. 2009, ARA&A, 47, 481, doi: 10.1146/annurev.astro.46.060407.145222

Astropy Collaboration, Robitaille, T. P., Tollerud, E. J., et al. 2013, A&A, 558, A33, doi: 10.1051/0004-6361/201322068

Astropy Collaboration, Price-Whelan, A. M., Sipőcz, B. M., et al. 2018, AJ, 156, 123, doi: 10.3847/1538-3881/aabc4f

Bailer-Jones, C. A. L., Rybizki, J., Fouesneau, M., Demleitner, M., & Andrae, R. 2021, AJ, 161, 147, doi: 10.3847/1538-3881/abd806

Ball, W. H., & Gizon, L. 2014, A&A, 568, A123, doi: 10.1051/0004-6361/201424325

Ball, W. H., Themeßl, N., & Hekker, S. 2018, MNRAS, 478, 4697, doi: 10.1093/mnras/sty1141

Basu, S., & Antia, H. M. 2004, ApJL, 606, L85, doi: 10.1086/421110

Belkacem, K., Goupil, M. J., Dupret, M. A., et al. 2011, A&A, 530, A142, doi: 10.1051/0004-6361/201116490

Benbakoura, M., Gaulme, P., McKeever, J., et al. 2021, arXiv e-prints, arXiv:2101.05351. https://arxiv.org/abs/2101.05351

Berger, T. A., Huber, D., van Saders, J. L., et al. 2020, AJ, 159, 280, doi: 10.3847/1538-3881/159/6/280

Brogaard, K., Hansen, C. J., Miglio, A., et al. 2018, MNRAS, 476, 3729, doi: 10.1093/mnras/sty268

Broomhall, A. M., Miglio, A., Montalbán, J., et al. 2014, MNRAS, 440, 1828, doi: 10.1093/mnras/stu393

Brown, T. M., Gilliland, R. L., Noyes, R. W., & Ramsey, L. W. 1991, ApJ, 368, 599, doi: 10.1086/169725

Casagrande, L., Flynn, C., Portinari, L., Girardi, L., & Jimenez, R. 2007, MNRAS, 382, 1516, doi: 10.1111/j.1365-2966.2007.12512.x

Casagrande, L., Lin, J., Rains, A. D., et al. 2021, MNRAS, 507, 2684, doi: 10.1093/mnras/stab2304

Choi, J., Dotter, A., Conroy, C., et al. 2016, ApJ, 823, 102, doi: 10.3847/0004-637X/823/2/102

Choi, J., Dotter, A., Conroy, C., & Ting, Y.-S. 2018, ApJ, 860, 131, doi: 10.3847/1538-4357/aac435

Chontos, A., Huber, D., Sayeed, M., & Yamsiri, P. 2021, arXiv e-prints, arXiv:2108.00582. https://arxiv.org/abs/2108.00582

Christensen-Dalsgaard, J. 2015, MNRAS, 453, 666, doi: 10.1093/mnras/stv1656

Cinquegrana, G. C., Joyce, M., & Karakas, A. I. 2023, MNRAS, 525, 3216, doi: 10.1093/mnras/stad2461

Claret, A., & Torres, G. 2018, ApJ, 859, 100, doi: 10.3847/1538-4357/aabd35

Coelho, H. R., Chaplin, W. J., Basu, S., et al. 2015, MNRAS, 451, 3011, doi: 10.1093/mnras/stv1175

[2] insert link upon publication.

878 Creevey, O. L., Metcalfe, T. S., Schultheis, M., et al. 2017,
879 A&A, 601, A67, doi: 10.1051/0004-6361/201629496
880 Cunha, M. S., Roxburgh, I. W., Aguirre Børsen-Koch, V.,
881 et al. 2021, MNRAS, 508, 5864,
882 doi: 10.1093/mnras/stab2886
883 Cutri, R. M., Skrutskie, M. F., van Dyk, S., et al. 2003,
884 2MASS All Sky Catalog of point sources.
885 Deheuvels, S., Brandão, I., Silva Aguirre, V., et al. 2016,
886 A&A, 589, A93, doi: 10.1051/0004-6361/201527967
887 Dréau, G., Cunha, M. S., Vrard, M., & Avelino, P. P. 2020,
888 MNRAS, 497, 1008, doi: 10.1093/mnras/staa1981
889 Eddington, A. S. 1926, The Internal Constitution of the
890 Stars (The University Press)
891 Epstein, C. R., Elsworth, Y. P., Johnson, J. A., et al. 2014,
892 ApJL, 785, L28, doi: 10.1088/2041-8205/785/2/L28
893 Gaulme, P., McKeever, J., Jackiewicz, J., et al. 2016, ApJ,
894 832, 121, doi: 10.3847/0004-637X/832/2/121
895 Gent, M. R., Bergemann, M., Serenelli, A., et al. 2022,
896 A&A, 658, A147, doi: 10.1051/0004-6361/202140863
897 Goldreich, P., Murray, N., & Kumar, P. 1994, ApJ, 424,
898 466, doi: 10.1086/173904
899 Green, G. M., Schlafly, E., Zucker, C., Speagle, J. S., &
900 Finkbeiner, D. 2019, ApJ, 887, 93,
901 doi: 10.3847/1538-4357/ab5362
902 Grevesse, N., & Sauval, A. J. 1998, SSRv, 85, 161,
903 doi: 10.1023/A:1005161325181
904 Hall, O. J., Davies, G. R., Elsworth, Y. P., et al. 2019,
905 MNRAS, 486, 3569, doi: 10.1093/mnras/stz1092
906 Hekker, S. 2020, Frontiers in Astronomy and Space
907 Sciences, 7, 3, doi: 10.3389/fspas.2020.00003
908 Henyey, L., Vardya, M. S., & Bodenheimer, P. 1965, ApJ,
909 142, 841, doi: 10.1086/148357
910 Herwig, F. 2000, A&A, 360, 952.
911 https://arxiv.org/abs/astro-ph/0007139
912 Ho, A. Y. Q., Rix, H.-W., Ness, M. K., et al. 2017, ApJ,
913 841, 40, doi: 10.3847/1538-4357/aa6db3
914 Howe, R., Chaplin, W. J., Basu, S., et al. 2020, MNRAS,
915 493, L49, doi: 10.1093/mnrasl/slaa006
916 Huber, D., Stello, D., Bedding, T. R., et al. 2009,
917 Communications in Asteroseismology, 160, 74.
918 https://arxiv.org/abs/0910.2764
919 Huber, D., Zinn, J., Bojsen-Hansen, M., et al. 2017, ApJ,
920 844, 102, doi: 10.3847/1538-4357/aa75ca
921 Hunter, J. D. 2007, Computing in Science & Engineering, 9,
922 90, doi: 10.1109/MCSE.2007.55
923 Jiang, C., Wu, T., Feinstein, A. D., et al. 2023, ApJ, 945,
924 20, doi: 10.3847/1538-4357/acb8ac
925 Jiménez, A., García, R. A., Pérez Hernández, F., &
926 Mathur, S. 2015, A&A, 583, A74,
927 doi: 10.1051/0004-6361/201526469
928 Jimenez, R., Flynn, C., MacDonald, J., & Gibson, B. K.
929 2003, Science, 299, 1552, doi: 10.1126/science.1080866
930 Joyce, M., & Chaboyer, B. 2018a, ApJ, 864, 99,
931 doi: 10.3847/1538-4357/aad464
932 —. 2018b, ApJ, 856, 10, doi: 10.3847/1538-4357/aab200
933 Joyce, M., Johnson, C. I., Marchetti, T., et al. 2023, ApJ,
934 946, 28, doi: 10.3847/1538-4357/acb692
935 Joyce, M., & Tayar, J. 2023, Galaxies, 11, 75,
936 doi: 10.3390/galaxies11030075
937 Kallinger, T. 2019, arXiv e-prints, arXiv:1906.09428.
938 https://arxiv.org/abs/1906.09428
939 Kallinger, T., Beck, P. G., Stello, D., & Garcia, R. A. 2018,
940 A&A, 616, A104, doi: 10.1051/0004-6361/201832831
941 Kallinger, T., Hekker, S., Mosser, B., et al. 2012, A&A,
942 541, A51, doi: 10.1051/0004-6361/201218854
943 Khan, S., Hall, O. J., Miglio, A., et al. 2018, ApJ, 859, 156,
944 doi: 10.3847/1538-4357/aabf90
945 Khan, S., Miglio, A., Mosser, B., et al. 2019, A&A, 628,
946 A35, doi: 10.1051/0004-6361/201935304
947 Kjeldsen, H., & Bedding, T. R. 1995, A&A, 293, 87.
948 https://arxiv.org/abs/astro-ph/9403015
949 Lebreton, Y., & Goupil, M. J. 2014, A&A, 569, A21,
950 doi: 10.1051/0004-6361/201423797
951 Lebreton, Y., Goupil, M. J., & Montalbán, J. 2014, in EAS
952 Publications Series, Vol. 65, EAS Publications Series, ed.
953 Y. Lebreton, D. Valls-Gabaud, & C. Charbonnel, 99–176,
954 doi: 10.1051/eas/1465004
955 Li, T., Bedding, T. R., Christensen-Dalsgaard, J., et al.
956 2020, MNRAS, 495, 3431, doi: 10.1093/mnras/staa1350
957 Li, T., Bedding, T. R., Huber, D., et al. 2018, MNRAS,
958 475, 981, doi: 10.1093/mnras/stx3079
959 Li, T., Li, Y., Bi, S., et al. 2022, ApJ, 927, 167,
960 doi: 10.3847/1538-4357/ac4fbf
961 Li, Y., Bedding, T. R., Stello, D., et al. 2021, MNRAS, 501,
962 3162, doi: 10.1093/mnras/staa3932
963 —. 2023, MNRAS, 523, 916, doi: 10.1093/mnras/stad1445
964 Lightkurve Collaboration, Cardoso, J. V. d. M., Hedges, C.,
965 et al. 2018, Lightkurve: Kepler and TESS time series
966 analysis in Python, Astrophysics Source Code Library.
967 http://ascl.net/1812.013
968 Magic, Z., Weiss, A., & Asplund, M. 2015, A&A, 573, A89,
969 doi: 10.1051/0004-6361/201423760
970 McKeever, J. M., Basu, S., & Corsaro, E. 2019, ApJ, 874,
971 180, doi: 10.3847/1538-4357/ab0c04
972 Metcalfe, T. S., Creevey, O. L., Doğan, G., et al. 2014,
973 ApJS, 214, 27, doi: 10.1088/0067-0049/214/2/27
974 Montalbán, J., Miglio, A., Noels, A., Scuflaire, R., &
975 Ventura, P. 2010, ApJL, 721, L182,
976 doi: 10.1088/2041-8205/721/2/L182

Montalbán, J., Mackereth, J. T., Miglio, A., et al. 2021, Nature Astronomy, 5, 640, doi: 10.1038/s41550-021-01347-7

Ong, J. M. J., & Basu, S. 2020, ApJ, 898, 127, doi: 10.3847/1538-4357/ab9ffb

Ong, J. M. J., Lund, M. N., Basu, S., et al. 2022, in Cambridge Workshop on Cool Stars, Stellar Systems, and the Sun, Cambridge Workshop on Cool Stars, Stellar Systems, and the Sun, 1, doi: 10.5281/zenodo.6685627

OpenAI. 2023, arXiv e-prints, arXiv:2303.08774, doi: 10.48550/arXiv.2303.08774

Paxton, B., Bildsten, L., Dotter, A., et al. 2011, ApJS, 192, 3, doi: 10.1088/0067-0049/192/1/3

Paxton, B., Cantiello, M., Arras, P., et al. 2013, ApJS, 208, 4, doi: 10.1088/0067-0049/208/1/4

Paxton, B., Marchant, P., Schwab, J., et al. 2015, ApJS, 220, 15, doi: 10.1088/0067-0049/220/1/15

Paxton, B., Schwab, J., Bauer, E. B., et al. 2018, ApJS, 234, 34, doi: 10.3847/1538-4365/aaa5a8

Paxton, B., Smolec, R., Schwab, J., et al. 2019, ApJS, 243, 10, doi: 10.3847/1538-4365/ab2241

Pinsonneault, M. H., Elsworth, Y. P., Tayar, J., et al. 2018, ApJS, 239, 32, doi: 10.3847/1538-4365/aaebfd

Sahlholdt, C. L., & Silva Aguirre, V. 2018, MNRAS, 481, L125, doi: 10.1093/mnrasl/sly173

Salaris, M., Cassisi, S., Schiavon, R. P., & Pietrinferni, A. 2018, A&A, 612, A68, doi: 10.1051/0004-6361/201732340

Samadi, R., Belkacem, K., Dupret, M. A., et al. 2012, A&A, 543, A120, doi: 10.1051/0004-6361/201219253

Schonhut-Stasik, J., Zinn, J. C., Stassun, K. G., et al. 2023, arXiv e-prints, arXiv:2304.10654, doi: 10.48550/arXiv.2304.10654

Sharma, S., Stello, D., Bland-Hawthorn, J., Huber, D., & Bedding, T. R. 2016, ApJ, 822, 15, doi: 10.3847/0004-637X/822/1/15

Silva Aguirre, V., Casagrande, L., Basu, S., et al. 2012, ApJ, 757, 99, doi: 10.1088/0004-637X/757/1/99

Silva Aguirre, V., Davies, G. R., Basu, S., et al. 2015, MNRAS, 452, 2127, doi: 10.1093/mnras/stv1388

Silva Aguirre, V., Lund, M. N., Antia, H. M., et al. 2017, ApJ, 835, 173, doi: 10.3847/1538-4357/835/2/173

Silva Aguirre, V., Stello, D., Stokholm, A., et al. 2020, ApJL, 889, L34, doi: 10.3847/2041-8213/ab6443

Smith, J. C., Stumpe, M. C., Van Cleve, J. E., et al. 2012, PASP, 124, 1000, doi: 10.1086/667697

Sreenivas, K. R., Bedding, T. R., Li, Y., et al. 2024, arXiv e-prints, arXiv:2401.17557. https://arxiv.org/abs/2401.17557

Stumpe, M. C., Smith, J. C., Van Cleve, J. E., et al. 2012, PASP, 124, 985, doi: 10.1086/667698

Tayar, J., Claytor, Z. R., Huber, D., & van Saders, J. 2022, ApJ, 927, 31, doi: 10.3847/1538-4357/ac4bbc

Tayar, J., Somers, G., Pinsonneault, M. H., et al. 2017, ApJ, 840, 17, doi: 10.3847/1538-4357/aa6a1e

Tian, Z., Bi, S., Bedding, T. R., & Yang, W. 2015, A&A, 580, A44, doi: 10.1051/0004-6361/201525968

Townsend, R. 2020, MESA SDK for Linux, 20.3.1, Zenodo, doi: 10.5281/zenodo.3706650

Townsend, R. H. D., & Teitler, S. A. 2013, MNRAS, 435, 3406, doi: 10.1093/mnras/stt1533

Valle, G., Dell'Omodarme, M., Prada Moroni, P. G., & Degl'Innocenti, S. 2019, A&A, 623, A59, doi: 10.1051/0004-6361/201834949

Valle, G., Dell'Omodarme, M., Tognelli, E., Prada Moroni, P. G., & Degl'Innocenti, S. 2018, A&A, 619, A158, doi: 10.1051/0004-6361/201833928

van der Walt, S., Colbert, S. C., & Varoquaux, G. 2011, Computing in Science and Engineering, 13, 22, doi: 10.1109/MCSE.2011.37

Verma, K., Raodeo, K., Basu, S., et al. 2019, MNRAS, 483, 4678, doi: 10.1093/mnras/sty3374

Viani, L. S., Basu, S., Chaplin, W. J., Davies, G. R., & Elsworth, Y. 2017, ApJ, 843, 11, doi: 10.3847/1538-4357/aa729c

Viani, L. S., Basu, S., Ong J., M. J., Bonaca, A., & Chaplin, W. J. 2018, ApJ, 858, 28, doi: 10.3847/1538-4357/aab7eb

Virtanen, P., Gommers, R., Oliphant, T. E., et al. 2020, Nature Methods, 17, 261, doi: https://doi.org/10.1038/s41592-019-0686-2

Vrard, M., Mosser, B., & Samadi, R. 2016, A&A, 588, A87, doi: 10.1051/0004-6361/201527259

Wang, C., Huang, Y., Zhou, Y., & Zhang, H. 2023a, A&A, 675, A26, doi: 10.1051/0004-6361/202245809

Wang, Y., Li, T., Bi, S., Bedding, T. R., & Li, Y. 2023b, ApJ, 953, 182, doi: 10.3847/1538-4357/ace4c9

Wes McKinney. 2010, in Proceedings of the 9th Python in Science Conference, ed. Stéfan van der Walt & Jarrod Millman, 56 – 61, doi: 10.25080/Majora-92bf1922-00a

Wu, Y., Xiang, M., Bi, S., et al. 2018, MNRAS, 475, 3633, doi: 10.1093/mnras/stx3296

Yıldız, M., Çelik Orhan, Z., & Kayhan, C. 2016, MNRAS, 462, 1577, doi: 10.1093/mnras/stw1709

Ying, J. M., Chaboyer, B., Boudreaux, E. M., et al. 2023, AJ, 166, 18, doi: 10.3847/1538-3881/acd9b1

Yu, J., Bedding, T. R., Stello, D., et al. 2020, MNRAS, 493, 1388, doi: 10.1093/mnras/staa300

Yu, J., Huber, D., Bedding, T. R., et al. 2018, ApJS, 236, 42, doi: 10.3847/1538-4365/aaaf74

Zhou, Y., Asplund, M., Collet, R., & Joyce, M. 2020, MNRAS, 495, 4904, doi: 10.1093/mnras/staa1445

1077 Zhou, Y., Christensen-Dalsgaard, J., Asplund, M., et al.
1078 2023, arXiv e-prints, arXiv:2310.20050,
1079 doi: 10.48550/arXiv.2310.20050

1080 Zinn, J. C., Pinsonneault, M. H., Bildsten, L., & Stello, D.
1081 2023, MNRAS, 525, 5540, doi: 10.1093/mnras/stad2560
1082 Zinn, J. C., Pinsonneault, M. H., Huber, D., et al. 2019,
1083 ApJ, 885, 166, doi: 10.3847/1538-4357/ab44a9